HYDROGEN, FUEL CELL & ENERGY STORAGE

A New SEPIC-Flyback DC-DC Converter for Fuel Cell Systems

Ali Janghorban | **Majid Delshad*** | **Bahador Fani**

Department of Electrical Engineering, Isf.C., Islamic Azad University, Isfahan, Iran
* Corresponding author, Email: delshad@khuisf.ac.ir

Article Information

Article Type
Research Article

Article History
Received: *12 Sep 2025*
Revised: *15 Oct 2025*
Accepted: *13 Dec 2025*
Published Online: *05 Jan 2026*

Keywords

SEPIC-flyback converter
Lossless snubber
Zero-voltage switching
Zero-current switching

Abstract

In this study, a SEPIC converter featuring a novel lossless snubber circuit is proposed for fuel cell applications. In the proposed topology, the main switch turns on under Zero-Current Switching (ZCS) conditions and turns off under Zero-Voltage Switching (ZVS), while all diodes experience Zero-Current turn-off, thereby eliminating reverse recovery issues. Moreover, the energy stored in the snubber circuit is transferred to the output, ensuring that the snubber does not introduce significant power loss to the system. The proposed snubber not only enables soft-switching operation but also enhances the voltage gain of the converter through the use of a three-winding transformer. Additionally, the absence of an auxiliary switch simplifies the control circuitry considerably. The converter has been implemented with a rated power of 200 W, and experimental results confirm the accuracy of both the PSPICE simulations and the theoretical analysis. Low input current ripple, high efficiency of 96.5%, and a switching frequency of 100 kHz make this converter highly suitable for fuel cell energy systems.

Cite this article: Janghorban, A., Delshad, M., Fani, B. (2026). A New SEPIC-Flyback DC-DC Converter for Fuel Cell Systems. DOI: 10.22104/hfe.2025.7747.1372

 Publisher: Iranian Research Organization for Science and Technology (IROST)
DOI: 10.22104/hfe.2025.7747.1372

1 Introduction

In energy generation systems based on fuel cells, the integration of efficient step-up DC–DC converters is of critical importance, as fuel cells typically produce low and load-dependent output voltages, usually ranging from 0.6 to 0.8 V per cell. A basic fuel cell consists of three main components: an anode, a cathode, and an electrolyte membrane [1–3]. In this electrochemical process, hydrogen is oxidized at the anode, releasing electrons and producing hydrogen ions, which travel through the electrolyte to the cathode where they react with oxygen to form water. This reaction simultaneously generates a continuous flow of electrical current. To achieve higher operating voltages suitable for practical applications, multiple cells are connected in series to form a fuel cell stack. From an electrical perspective, a fuel cell can be modeled as a nonlinear voltage source whose output voltage depends on the current and includes losses due to activation, ohmic resistance, and mass transport (concentration). These factors result in a nonlinear, descending current–voltage (I–V) curve under load conditions. As a result, the interface converter must be designed with these characteristics in mind. It must also provide a high voltage conversion ratio, low input current ripple (to avoid damaging the fuel cell), and high efficiency under high switching frequency operation [4–6].

To reduce the size, weight, and cost of magnetic and passive components in DC–DC converters, increasing the switching frequency is a widely adopted approach. A higher switching frequency allows for the use of smaller inductors and capacitors, thereby enhancing the power density of the converter [7,8]. However, this advantage comes at a cost. One of the primary challenges is the increase in switching losses, which result from rapid transitions in voltage and current across the semiconductor devices. These elevated switching losses not only degrade the overall efficiency of the converter but also lead to higher electromagnetic interference (EMI), which can adversely affect the operation of nearby electronic systems and complicate the design of electromagnetic compatibility [9].

To mitigate these issues, numerous auxiliary circuits have been proposed in the literature with the goal of enabling soft-switching conditions such as Zero Voltage Switching (ZVS) [10] or Zero Current Switching (ZCS) [11] to reduce switching losses and improve efficiency. However, many of these auxiliary networks suffer from drawbacks. For instance, some configurations result in increased voltage stress on the main switch or the rectifier diodes, necessitating the use of higher-rated (and more expensive) components and potentially introducing additional conduction losses [12]. Moreover, auxiliary circuits that rely on extra switching devices can compromise the reliability and cost-effectiveness of the overall system [13]. Therefore, the most effective auxiliary circuits are those that achieve soft switching while maintaining low circulating currents and avoiding additional switches, thus ensuring a compact, efficient, and reliable converter design [14]. In [15], a novel ultra-high step-up converter using a self-switched inductor technique and a voltage multiplier circuit is presented. This topology features low voltage stress on the switch; however, the high number of components increases the complexity of the converter operation. On the other hand, in [16], a coupled-inductor-based converter with an interleaved structure is proposed. Despite its advantages, this topology suffers from uneven thermal distribution across the phases and hard-switching, which are major drawbacks. This research presents a new soft-switching SEPIC-flyback converter that enables efficient switching performance through the integration of a properly designed lossless snubber circuit while maintaining a minimal component count. The converter continues to operate under a conventional PWM control scheme, ensuring simplicity and compatibility with standard control methods. The proposed snubber facilitates ZCS during the turn-on transition and ZVS during turn-off of the main switch, effectively minimizing switching losses. Furthermore, the converter's diodes are turned off under ZCS conditions, thereby eliminating reverse recovery issues and enhancing overall efficiency. Compared to typical active-clamp configurations, the proposed snubber introduces significantly lower circulating current, ensuring that no substantial conduction losses are imposed on the system.

In this study, section 2 presents the configuration of the proposed converter along with a comprehensive explanation of its operational behavior. In section 3, a thorough analytical study of the converter is carried out to investigate its performance characteristics. Section 4 includes simulation results obtained using PSPICE to verify the theoretical predictions. To further support the analysis, a hardware prototype is constructed and tested. Lastly, section 5 offers a performance comparison between the proposed design and other contemporary converter topologies, demonstrating its relative advantages.

2 The Proposed Step-Up Converter

In this section, the proposed converter is presented with a detailed explanation of its operation. The fundamen-

tal working principles and the specific circuit topology are carefully examined and described to offer a clear and thorough understanding of how the converter functions.

2.1 Proposed converter description

Figure 1 presents the structure of the proposed SEPIC–flyback converter. The topology is composed of the main switch M, capacitors C, C_{o1}, and C_{o2}, inductors L_1 and L_2, along with diodes D_{o1} and D_{o2}. The associated snubber circuit incorporates diodes D_{a1}, D_{a2}, and D_{a3}, a snubber capacitor C_r to achieve zero-voltage turn-off (ZV turn-off) for the main switch, and inductor L_{a1} to enable zero-current turn-on (ZC turn-on). Additionally, coupled inductors L_{a2}–L_{a3} and L_{a4} are utilized to deliver the snubber energy to the output.

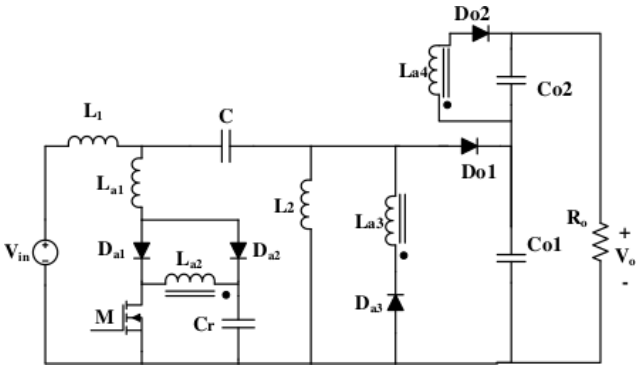

Fig. 1. Schematic of the proposed high step-up

2.2 Converter operation

Figure 2 presents the essential waveforms of the converter. The operation of the converter consists of six different states during each switching cycle. To simplify the analysis, voltage changes across the capacitors C and C_o are ignored, and all components are assumed to be ideal. The equivalent circuits corresponding to each state are depicted in Figure 3. Prior to the first state, the switch M remains off, the output diode D_o is conducting, and the inductor L_2 discharges linearly into the load.

Prior to the first state, switch M remains off, the output diode D_{o1} is forward-biased, and inductor L_2 discharges linearly into the load

Mode 1: The cycle starts when the switch M is activated with zero-current switching, facilitated by the series inductor L_a. During this interval, the output diode D_o remains in conduction mode, resulting in the voltage sum of $V_o + V_{C_{o1}}$ appearing across L_a. This causes the current through the switch to rise steadily. Concurrently, diode D_{a1} conducts, carrying a current profile similar to that of the main switch.

Mode 2: Following the turn-off of the output diode D_o under zero-current conditions, a resonant interaction occurs between the snubber capacitor C_r and the inductor L_{a1}. This resonance transfers the stored energy from C_r to L_{a1}, completing after roughly a quarter of the switching period when C_r is fully discharged.

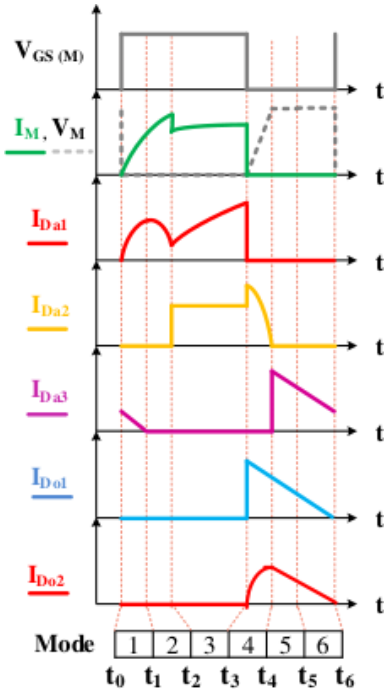

Fig. 2. Main waveforms of the proposed converter

Mode 3: When the voltage across the capacitor C_r reaches zero, diode D_{a2} becomes forward biased, effectively short-circuiting the inductor L_{a2}. This action keeps the voltage on C_r at zero volts, while the output capacitor takes over supplying power to the load.

Mode 4: This phase commences with the switch M turning off, allowing the capacitor C_r to charge linearly, thereby enabling a zero-voltage turn-off condition. In addition, diode D_{a3} turns on, permitting the energy stored in L_{a2} to transfer to the output via magnetic coupling with L_{a3} and conduction through D_{a3}. This mechanism ensures that the snubber energy is recycled efficiently rather than dissipated as losses.

Mode 5: Once the energy stored in L_{a1} is exhausted, diode D_{a2} switches off under zero-current conditions. At the same time, the output diode D_o turns on, and inductor L_2 begins discharging its energy into the load. This Mode continues until the energy in L_{a2} is fully depleted.

Mode 6: With the complete depletion of energy in L_{a2}, diode D_{a3} turns off, marking the start of the final Mode. The output diode D_o remains active, enabling inductor L_2 to keep delivering energy to the load, while inductor L_1 discharges into the capacitor C.

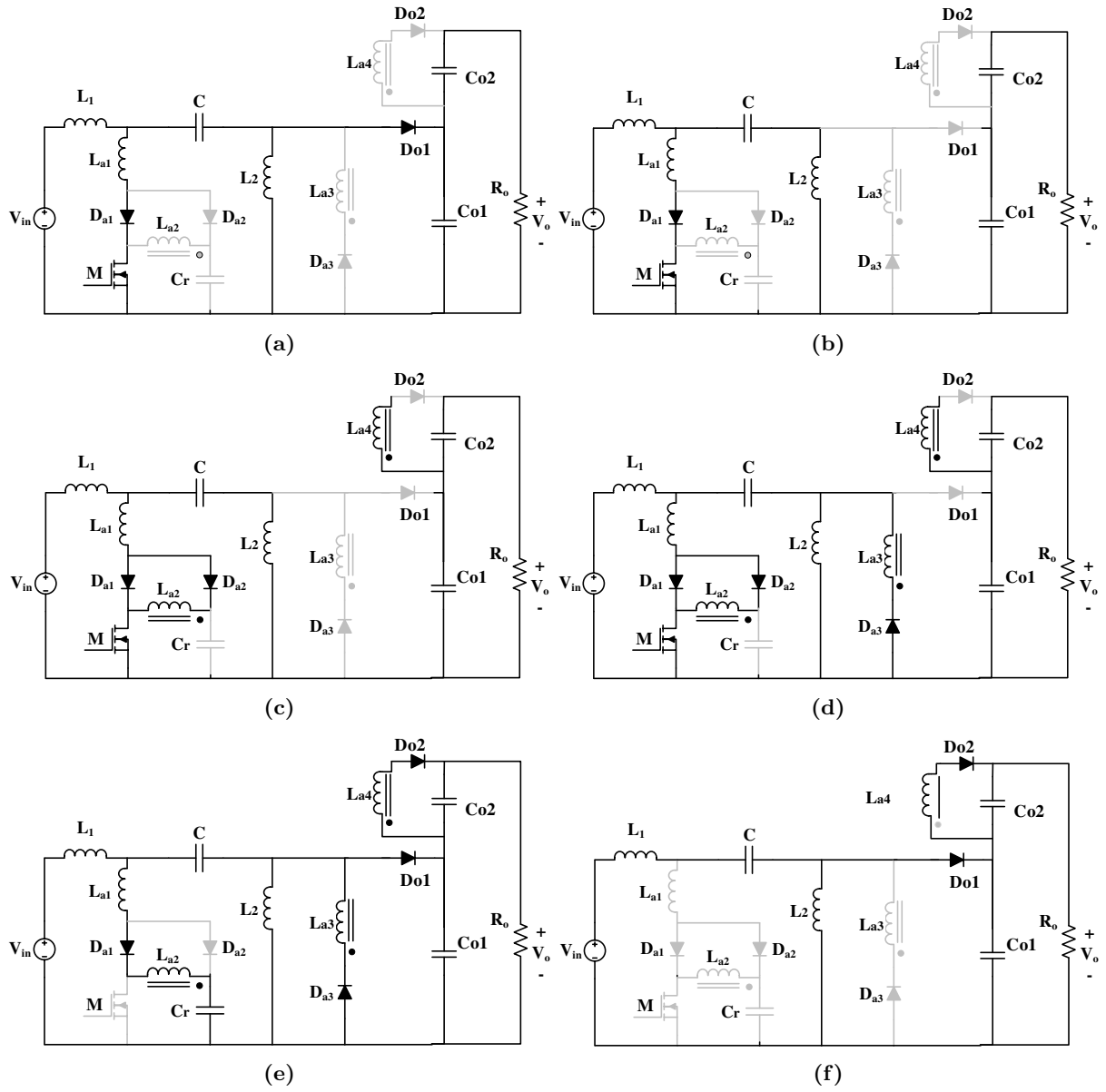

Fig. 3. Equivalent circuitry is derived for each mode (a) Mode 1 (b) Mode 2 (c) Mode 3 (d) Mode 4 (e) Mode 5 (f) Mode 6

3 Analysis of the Proposed SEPIC–Flyback Converter

As discussed in the previous section, the snubber circuit not only facilitates soft-switching conditions for the power switch but also significantly contributes to enhancing the overall efficiency of the converter. By recovering the energy stored in its components, the snubber circuit reduces switching losses and improves the converter's power transfer capability. In this topology, the energy recovered from the snubber circuit is transferred to the voltage lift capacitor (C_{o2}) through the magnetically coupled three winding transformer, thereby contributing to its charging process. This mechanism enhances energy utilization and minimizes power dissipation within the system.

In the following section, the design methodology for the key converter components such as inductors, capacitors, the transformer, and control elements will be detailed. Furthermore, essential operational parameters, including voltage gain, current ripple, and switching conditions, will be analyzed and discussed.

3.1 Converter gain

The voltage gain of the proposed topology can be derived by applying volt-second balance on the input inductor and magnetizing inductor. The resulting gain is:

$$\text{for } \mathrm{L}_1 : V_{\mathrm{in}}DT + (V_{\mathrm{in}} - V_{\mathrm{C_r}})(1-D)T = 0\,, \tag{1}$$

$$V_{\mathrm{C_{r1}}} = \frac{V_{\mathrm{in}}}{1-D}\,, \tag{2}$$

$$\text{for } \mathrm{L}_2 : -V_C DT + (V_{\mathrm{C_{o1}}})(1-D)T = 0\,, \tag{3}$$

$$V_{\mathrm{C_{o1}}} = \frac{DV_C}{1-D} \xrightarrow{V_C = V_{\mathrm{in}}} V_{CO1} = \frac{DV_{\mathrm{in}}}{1-D}\,, \tag{4}$$

$$\text{for } \mathrm{L}_m : kV_{\mathrm{C_r}}DT + \left(-\frac{V_{\mathrm{C_{o2}}}}{n}\right)(1-D)T = 0\,, \tag{5}$$

$$V_{\mathrm{C_{o2}}} = \frac{nkDV_{\mathrm{in}}}{(1-D)^2}\,, \tag{6}$$

$$k = \frac{L_m}{L_m + L_k}\,, \tag{7}$$

$$V_o = V_{\mathrm{C_{o1}}} + V_{\mathrm{C_{o2}}}\,, \tag{8}$$

$$\frac{V_o}{V_{\mathrm{in}}} = \frac{(nk+1)D - D^2}{1-D}\,, \tag{9}$$

where n is turn ratio, D is duty cycle, k is coupling coefficient, T is switching period.

Under the ideal condition of $k = 1$, the gain can be expressed as

$$\frac{V_o}{V_{\mathrm{in}}} = \frac{(n+1)D - D^2}{1-D} \tag{10}$$

Figures 4 and 5 illustrate the variation of the converter's voltage gain with respect to the coupling coefficient and the turns ratio, respectively.

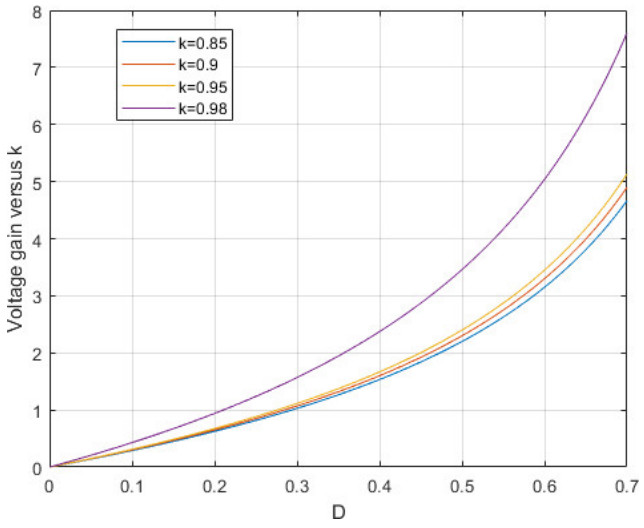

Fig. 4. Converter gain diagram based on variations in the duty cycle and coupling factor.

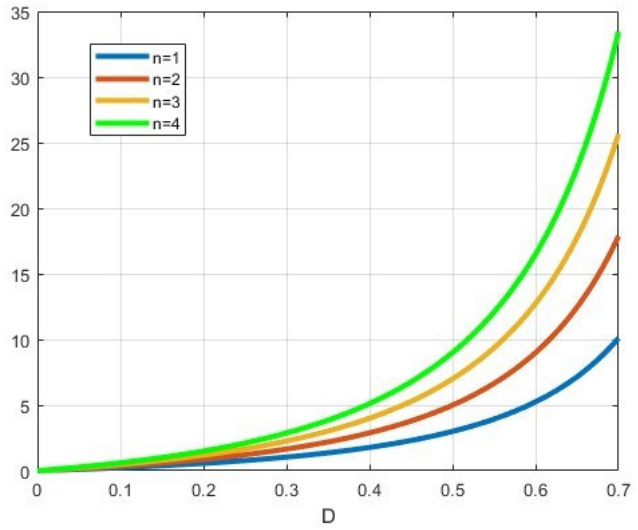

Fig. 5. Converter gain diagram based on variations in the duty cycle and turn ratio.

3.2 Voltage stress on components

The voltage stress on the semiconductor devices can be determined using Kirchhoff's Voltage Law (KVL) in both input and output loops during the off-Mode of the respective devices. The resulting expressions are:

$$V_M = \frac{V_{\mathrm{in}}}{1-D} + \frac{V_{\mathrm{in}}D}{(1-D)^2} = \frac{V_o}{(n+1)D - D^2} \tag{11}$$

$$V_{\mathrm{D_{o1}}} = \frac{V_{\mathrm{in}}}{1-D} = \frac{(1-D)V_o}{(n+1)D - D^2} \tag{12}$$

$$V_{\mathrm{D_{o2}}} = \frac{nDV_o}{(n+1)D - D^2)} \tag{13}$$

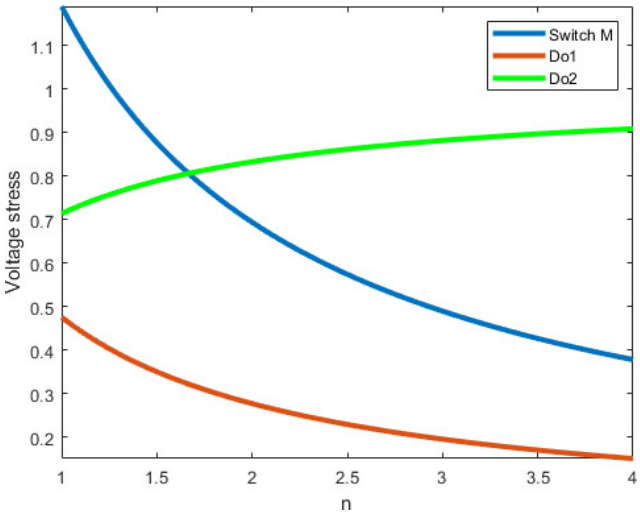

Fig. 6. Normalized stress diagram of the converter's switch and output diodes.

3.3 Design of snubber capacitor (C_r)

To achieve soft switching and suppress voltage overshoots, snubber capacitors are dimensioned according to the energy that must be absorbed during switching events. Their capacitance is determined by considering the current through the switch, the post-turn-off voltage, and the duration of the switching transition. An appropriate design of these capacitors helps reduce switching losses and enhances the converter's overall efficiency.

$$C_r = \frac{I_{\text{sw}} t_f}{2V_{\text{sw}}} \tag{14}$$

Where I_{sw} is the switch current, V_{sw} represents the switch voltage after turn-off, while t_f denotes the fall time of the switch current.

3.4 Design of snubber inductor

Snubber inductors, connected in series with the main switches, are employed to limit the rate of change of the switching current. Their inductance values are selected based on the voltage applied across the switches and the desired current rise time during turn-on.

$$L_{\text{a1}} = \frac{V_{\text{sw}} t_r}{I_{\text{sw}}} \tag{15}$$

here t_r denotes the time interval during which the switch current rises from zero to its maximum value.

3.5 Design of output capacitors and inductors

The magnetizing inductor, along with L_1 and L_2, is designed to store energy and control current ripple in accordance with the specified operating conditions. Their inductance values are selected to maintain stable converter performance and to reduce variations in energy transfer.

$$L_m = \frac{V_{\text{cr}} D}{\Delta I_{\text{Lm}} f} = \frac{V_{\text{in}} D}{\Delta I_{\text{Lm}} f(1-D)}, \tag{16}$$

$$L_{1,2} = \frac{V_{\text{in}} D}{\Delta I_L f} \tag{17}$$

where f is switching frequency, ΔI_{Lm} is current ripple of magnetizing inductor.

Likewise, the output capacitors are chosen to efficiently attenuate voltage ripple and ensure a stable DC output. Their capacitance is determined based on the acceptable output voltage ripple and the load resistance, ensuring smooth and reliable voltage regulation.

$$C = \frac{D I_{\text{L2}}}{\Delta V_c f} \tag{18}$$

$$\text{C}_{\text{o1}} = \frac{D I_{\text{L2}}}{\Delta V_{\text{C}_{\text{o1}}} f} \tag{19}$$

$$\text{C}_{\text{o2}} = \frac{D I_{\text{L1}}}{n \Delta V_{\text{C}_{\text{o2}}} f} \tag{20}$$

where ΔV_c is voltage ripple of capacitor C, $\Delta V_{\text{C}_{\text{o1}}}$ is voltage ripple of capacitor C_{o1} and $\Delta V_{\text{C}_{\text{o2}}}$ is voltage ripple of capacitor C_{o2}.

4 Simulation Results

To validate the accuracy of the analytical results presented in the previous sections, the proposed converter was designed and subsequently simulated using PSPICE software. The specifications and component values of the designed converter are summarized in Table 1. Based on the theoretical analysis discussed earlier, the converter components were selected for a target power output of 200 W and the corresponding simulation was performed. Figure 7a illustrates the simulated voltage and current waveforms of the main switch M in the proposed converter. As observed, the switch current rises gradually at turn-on, indicating a Zero-Current switching condition. Similarly, at turn-off, the voltage increases with a slope, reflecting a Zero-Voltage turn-off condition.

The current waveforms of diodes D_{a1} and D_{a2} are shown in Figure 7b. Their currents decrease gradually to zero during turn-off, confirming ZC turn-off behavior and indicating that reverse recovery issues are avoided. Figure 7c presents the output diodes current waveforms, which also exhibit ZC turn-off characteristics. This implies that these diodes similarly operate without encountering reverse recovery problems.

Table 1. Fundamental design attributes of the converter

Specification/element	Part no./Value
V_{in}	40 V
V_o	360 V
P_O	200 W
f_S	100 kHz
switch	IPW60R041C6
All diodes	STTH8R04
L_1, L_2	$200 - 400\,\mu$H
L_{a1}	$10\,\mu$H
L_{a2}- L_{a3}- L_{a4}	$40 - 200 - 800\,\mu$H
C	$10\,\mu$F
C_r	4 nF
C_{o1}-C_{o2}	$10\,\mu$F

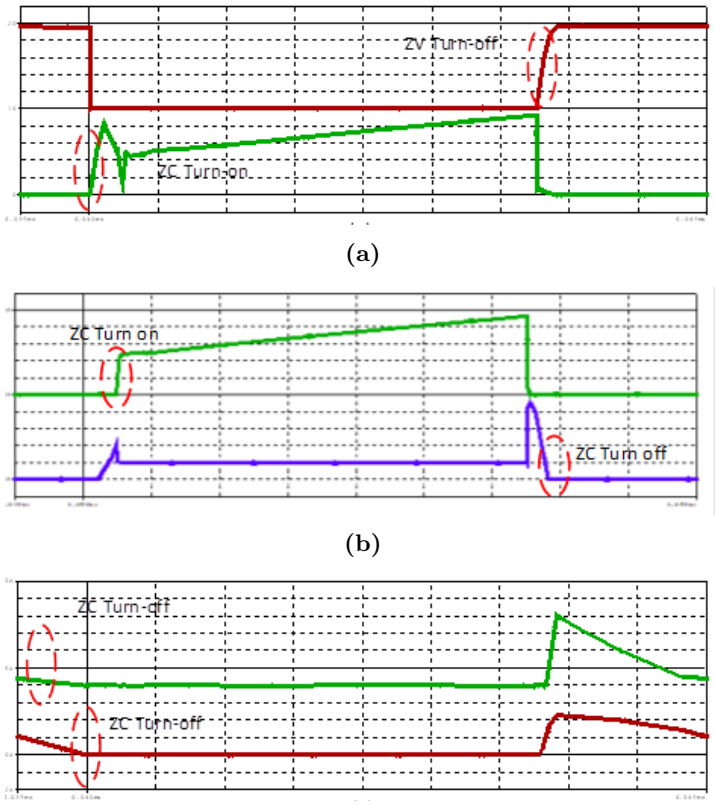

Fig. 7. Simulation results (a) voltage (top) and current (bottom) waveforms of switch M, (1 μs/div, 2 A/div, 50 V/div) **(b) current waveform of** D_{a1} **(top) and current waveform of** D_{a2} **(bottom),** (1 μs/div, 2 A/div) **(c) current waveform of** D_{o1} **(top) and current waveform of** D_{o2} **(bottom),** (1 μs/div, 1 A/div)**.**

5 The experimental Results

Figure 8a shows the prototype of the converter operating at 200 W. As can be seen, the implemented converter features a compact size and reduced volume, mainly due to its high switching frequency of 100 kHz. Figure 8b illustrates the experimental waveforms of the voltage and current of the switch. These results confirm the simulation outcomes and demonstrate that Zero-Current (ZC) turn-off is achieved. Additionally, the voltage stress on the switch remains below the output voltage, which contributes to reduced conduction losses, lower cost, and improved reliability. The observed oscillations during switch turn-off are attributed to the resonance between the transformer's leakage inductance and the parasitic capacitance of the switch. Figure 8c presents the current waveforms of diodes D_{a1} and D_{a2}. According to the measured results, both diodes achieve Zero-Current Switching (ZCS) during turn-on. Figure 8d shows the current waveforms of the output diodes D_{o1} and D_{o2}. As evident, these diodes are turned off under ZCS conditions, thus eliminating reverse recovery issues. The limited unwanted oscillations observed during diode turn-off are caused by the resonance between leakage inductance and the diodes' parasitic capacitance. These oscillations can be mitigated by reducing the leakage inductance.

6 Loss Analysis of the Proposed Converter

In this section, the impact of semiconductor components on the overall power performance of the proposed converter is evaluated. The conduction losses of MOSFETs, diodes, coupled inductors, and capacitors are taken into account. Since the converter operates under soft-switching conditions with Zero Current Switching (ZCS) for the main switch, capacitive turn-on losses are present, but switching losses remain negligible.

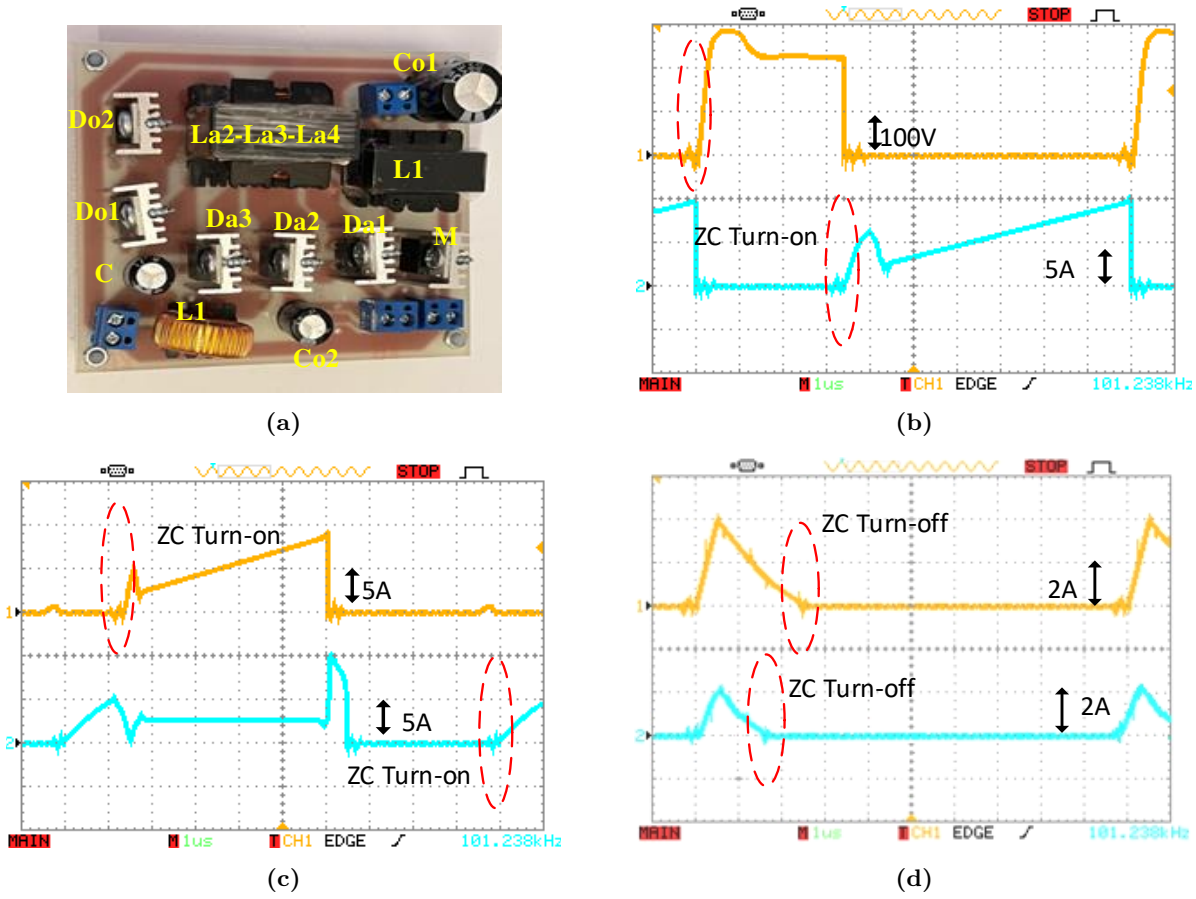

Fig. 8. The practical results (a) implemented circuit (b)waveforms of the drain-source voltage (up) and the current (bottom) in the switch M (c) waveforms of the drain-source voltage (up) and the current (bottom) in the switch S_2 (d) current waveforms of diodes $\mathrm{D_{a1}}$ (bottom) and $\mathrm{D_{o1}}$ (up) (e) current waveforms of diodes D_1 (bottom) and D_2 (up)

The conduction losses of the switches depend on the drain-source resistance and their RMS currents. The capacitive turn-on losses are influenced by the switch's output capacitance (Coss), operating frequency (fs), and the voltage across the switch (Vs). Based on these factors, the total loss of the power switches is calculated accordingly.

$$R_{\mathrm{DS}}(\mathrm{on}) \times I^2_{\mathrm{RMS},M} + \frac{1}{2} C_{\mathrm{oss}} V_S^2 f_s = 0.04 \times 40.06 + 0.5 \times 780 \times 10^{-12} \times 62500 \times 10^5 = 2.76\,\mathrm{W} \quad (21)$$

The conduction losses of the diodes are related to their forward voltage drop (VF) and the average current passing through them. These values are used to estimate the total diode losses.

$$V_{F,\mathrm{D_{a1}}} I_{\mathrm{av},\mathrm{D_{a1}}} + V_{F,\mathrm{D_{a2}}} I_{\mathrm{av},\mathrm{D_{a2}}} + V_{F,\mathrm{D_{a3}}} I_{\mathrm{av},\mathrm{D_{a3}}} + V_{F,\mathrm{Do1}} I_{\mathrm{av},\mathrm{Do1}} + V_{F,\mathrm{Do2}} I_{\mathrm{av},\mathrm{Do2}} = 0.85 \times 4.56 = 3.27\,\mathrm{W} \quad (22)$$

Similarly, the conduction losses of the inductors are calculated by considering the winding resistance and the RMS currents through each inductor.

$$R_{\mathrm{DC,La_2}} I^2_{\mathrm{RMS,La_2}} + R_{\mathrm{DC,La_3}} I^2_{\mathrm{RMS,La_3}} + R_{\mathrm{DC,La_4}} I^2_{\mathrm{RMS,La_4}} + R_{\mathrm{DC,L1}} I^2_{\mathrm{RMS,L1}} + R_{\mathrm{DC,L2}} I^2_{\mathrm{RMS,L2}} = 1.06\,\mathrm{W} \quad (23)$$

For the capacitors, the losses are estimated by considering their equivalent series resistance (ESR) and the associated RMS currents.

$$\mathrm{ESR}_C \times I^2_{\mathrm{RMS},C} + \mathrm{ESR}_C \times I^2_{\mathrm{RMS},C_{o1}} + \mathrm{ESR}_C \times I^2_{\mathrm{RMS},C_{o2}} = 0.82\,\mathrm{W} \quad (24)$$

Based on the overall analysis, the total power loss in the proposed 200 W converter is approximately 7.91 W, resulting in an overall efficiency of 96.2%. The distribution of power losses among the converter components is illustrated in Figure 9.

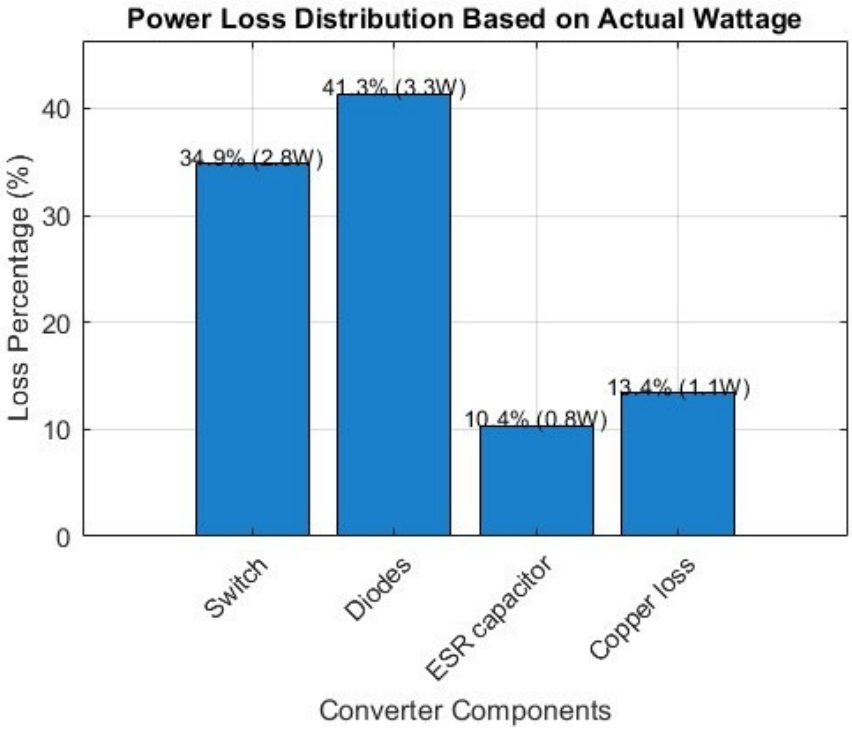

Fig. 9. Distribution loss in components

7 Measured Efficiency of the Proposed Converter

The efficiency of the proposed converter is illustrated in Figure 10. As shown, the converter achieves an efficiency of 96.2% at full load. It is worth noting that the efficiency decreases at lower power levels. This reduction is mainly due to the fact that, in the proposed converter, the snubber circuit also serves as a power transfer path. At light load conditions, the circulating current in the snubber does not significantly decrease, which leads to lower overall efficiency.

8 A Comparative Analysis Between the Proposed Converter and Similar Topologies

In this section, a comparative assessment is carried out between the proposed converter and earlier similar designs, focusing on parameters including component count, achievable voltage gain, peak voltage stress, continuity of input current, switching technique, and other pertinent performance aspects, as presented in Table 2.

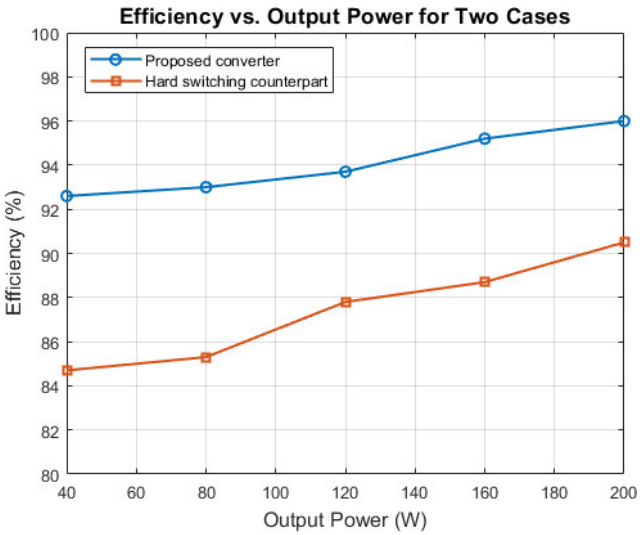

Fig. 10. Efficiency comparison of the proposed step-up converter with its hard-switching counterpart

As indicated in Table 2, both the proposed converter and Converter [14] utilize the lowest number of components among the compared topologies. Nevertheless, the proposed converter offers distinct advantages over Converter [14], including a reduced number of switches and a lower input current ripple. Although Converters [17] and [18] achieve higher voltage gains, Converter [17] incorporates a larger num-

Table 2. Comparative analysis table for the proposed converter

Converter	Voltage gain	Maximum voltage stress across switch	Maximum voltage stress across diode	No. of elements					Switching condition	Input current ripple
				S	M.C[1]	D	C	T[2]		
[12]	$\frac{2+n+D(n-1)}{1-D}$	$\frac{V_o}{2+n+D(n-1)}$	$\frac{1+n+D(n-1)V_o}{2+n+D(n-1)}$	2	2	4	4	12	ZVS	High
[14]	$\frac{2n}{(1-D)}$	$\frac{V_o}{2n}$	$\frac{(2n-D)V_o}{2n}$	3	3	3	6	15	ZCS	Low
[15]	$\frac{1+2nD}{1-D}+2n$	$\frac{V_o}{1+2nD}$	$\frac{nV_o}{1+2nD}$	1	2	5	6	14	ZCS	Low
[19]	$\frac{1+n(D+2)}{1-D}$	$\frac{V_o}{1+n(D+2)}$	$\frac{nV_o}{1+n(D+2)}$	2	1	5	6	14	ZVS	High
[17]	$\frac{1+n(2-D)^2)}{(1-D)^2}$	$\frac{V_o}{1+n(2-D)^2}$	$\frac{(1-D)V_o}{1+n(2-D)^2}$	2	3	5	6	16	Hard	High
[18]	$\frac{1+2n}{1-D}$	$\frac{V_o}{1+2n}$	$\frac{nV_o}{1+2n}$	2	2	4	6	14	ZVS	Low
Proposed Converter	$\frac{(n+1)D-D^2}{1-D}$	$\frac{V_o}{(n+1)D-D^2}$	$\frac{nV_o}{1+2n}$	1	3	5	3	12	ZCS	Low

ber of components and exhibits higher input current ripple, which not only increases the implementation cost but also renders it less suitable for fuel cell applications. Converter [18] employs an active-clamp technique to facilitate soft-switching; however, this approach introduces challenges such as elevated current stress on components and the loss of soft-switching capability under light-load conditions. Converter [19], in addition to its higher component count, also suffers from increased input current ripple, leading to similar drawbacks as Converter [17]. Converter [15] demonstrates soft-switching operation and low input current ripple comparable to the proposed converter and employs only a single switch; however, it lacks a common ground between the input and output, which may limit its applicability in certain systems.

9 Conclusions

This study proposed a new SEPIC–flyback converter with a lossless snubber circuit for fuel cell applications. The converter enables soft-switching operation for the main switch, such that it turns on under Zero-Current Switching (ZCS) and turns off under Zero-Voltage Switching (ZVS). The diodes also turn off under ZCS conditions, effectively eliminating reverse recovery issues. The absence of an auxiliary switch simplifies the control circuitry, and the energy stored in the snubber is fully transferred to the output, resulting in higher overall efficiency. The converter employs simple PWM-based control and allows for higher switching frequencies, leading to reduced volume and weight. Furthermore, the continuous input current reduces stress on the fuel cell and contributes to an extended operational lifetime. Nevertheless, the proposed converter has two notable drawbacks. First, capacitive turn-on losses occur due to the inherent parasitic capacitance of the switch. Second, voltage overshoot may arise as a result of the series inductor present in the snubber path. These limitations must be considered in the practical implementation and component selection of the converter design. Experimental results obtained from the prototype demonstrate an input current ripple of approximately 1A and an efficiency of 96.2% at an output power of 200W, which make the proposed design well-suited for fuel cell applications.

References

[1] Sareban R, Amini M, Delshad M, Yazdani MR. An Improved Zero Current Transition High Step-Up Single-Switch Converter for Fuel Cell Applications;.

[2] Farzad MA, Hassanzadeh H. Non-Isothermal Modeling of Planar Solid Oxide Fuel Cell. Hydrogen, Fuel Cell & Energy Storage. 2025;12(2):135-

[1] Magnetic Core
[2] Total number of elements

48.

[3] Chen L, Rong D, Sun X. A family of high step-up soft-switching integrated sepic converter with Y-source coupled inductor. IEEE Access. 2023;11:111752-64.

[4] Li H, Chen Y, Jin T. A soft-switched sepic-based high voltage gain DC–DC converter for renewable energy applications. IEEE Transactions on Industrial Electronics. 2024.

[5] Jafari H, Hassanzadeh H. Investigation of a fuel cell (FC) system for vehicle. Hydrogen, Fuel Cell & Energy Storage. 2024;11(4):259-70.

[6] Rahimi-Esbo M, Dadashi Firouzjaei K, Ghasemian M. New criterion for achieving efficient flow fields in PEM fuel cells. Hydrogen, Fuel Cell & Energy Storage. 2024;11(1):46-67.

[7] Murad Z, Al Anzi F, Ben-Brahim L. A comparative study of high-gain cascaded DC-DC converter topologies. In: 2022 3rd International Conference on Smart Grid and Renewable Energy (SGRE). IEEE; 2022. p. 1-6.

[8] Ding X, Jiang K, Yu Y, Li B, Sun Y, Quan L. A high step-up DC–DC converter integrated with modified sepic network. IEEE Transactions on Industrial Electronics. 2024.

[9] Hashemzadeh SM, Al-Hitmi MA, Aghaei H, Marzang V, Iqbal A, Babaei E, et al. An ultra-high voltage gain interleaved converter based on three-winding coupled inductor with reduced input current ripple for renewable energy applications. IET Renewable Power Generation. 2024;18(1):141-51.

[10] Delshad M, Farzanehfard H. A soft switching flyback current-fed push pull DC-DC converter with active clamp circuit. In: 2008 IEEE 2nd International Power and Energy Conference. IEEE; 2008. p. 203-7.

[11] Delshad M, Shahri E. A new soft switching interleaved boost converter with high voltage gain. In: The 8th Electrical Engineering/Electronics, Computer, Telecommunications and Information Technology (ECTI) Association of Thailand-Conference 2011. IEEE; 2011. p. 744-7.

[12] Karimi Hajiabadi M, Mosallanejad A, Salemnia A. Ultra-high gain quadratic boost DC–DC converter based on a three-winding coupled inductor with reduced voltage stress for fuel cell-based systems. IET Power Electronics. 2023;16(16):2666-81.

[13] Alizadeh D, Babaei E, Sabahi M. High step-up quadratic impedance source DC-DC converter based on coupled inductor. IEEE Journal of Emerging and Selected Topics in Power Electronics. 2022;11(6):5930-9.

[14] Zhang G, Chen H, Yu SS, Jin N, Zhang Y. Generalized flexible voltage pumping module for extra high voltage gain converters in electric vehicles. IEEE Transactions on Vehicular Technology. 2021;70(7):6463-71.

[15] Rajesh R, Prabaharan N, Hossain E. Design and analysis of a new high step-up converter using switched-inductor-capacitor voltage multiplier cells for photovoltaic application. IEEE Journal of the Electron Devices Society. 2023;12:842-8.

[16] Hashemzadeh SM, Babaei E, Hosseini SH, Sabahi M. Design and analysis of a new coupled inductor-based interleaved high step-up DC-DC converter for renewable energy applications. International Transactions on Electrical Energy Systems. 2022;2022(1):7618242.

[17] Siwakoti YP, Blaabjerg F, Loh PC. High step-up trans-inverse (Tx- 1) DC–DC converter for the distributed generation system. IEEE Transactions on Industrial Electronics. 2016;63(7):4278-91.

[18] Gohari HS, Abbasian S, Mardakheh NA, Abbaszadeh K, Blaabjerg F. Coupled inductor-based current-fed ultra-high step-up DC-DC converter featuring low input current ripple. IEEE Transactions on Circuits and Systems II: Express Briefs. 2022;71(2):887-91.

[19] Hasanpour S, Lee SS. New step-up DC/DC converter with ripple-free input current. IEEE Transactions on Power Electronics. 2023;39(2):2811-21.